



Hydrothermal synthesis of halloysite nanotubes @carbon nanocomposites with good biocompatibility

Jun Zhang, Tengfei Liu, Mingxian Liu*

Department of Materials Science and Engineering, Jinan University, Guangzhou, 510632, China



ARTICLE INFO

Keywords:

Halloysite nanotubes
Carbonization
Hydrothermal
Adsorption
Biocompatibility

ABSTRACT

In this work, the halloysite nanotubes@carbon (HNTs@C) nanocomposites are synthesized by one-step hydrothermal carbonization of glucose on the surface of HNTs. HNTs can effectively induce heterogeneous deposition of carbonaceous materials on their surfaces, which leads to a layer of amorphous carbon around HNTs. The HNTs@C was characterized by transmission electron microscopy, scanning electron microscopy, Fourier transform infrared spectroscopy, X-ray diffraction, and X-ray photoelectron spectroscopy. The influence of glucose loading and reaction time on the structure of nanocomposite was investigated. The thickness of carbon on the surface of HNTs increases with the increase of glucose loading and reaction time. The bovine serum albumin adsorption experiments show that HNTs@C has stronger protein adsorption ability than raw HNTs. Hemolysis experiments show that HNTs@C exhibits decreased hemolysis rate in comparison to HNTs. The *in vitro* cell culture experiments using HeLa cells reveal that HNTs@C has lower cytotoxicity than raw HNTs. All of these indicate that HNTs@C has good adsorption capacity and biocompatibility, and they have potential applications in biomedical areas such as drug delivery carrier.

1. Introduction

In recent years, as a new type of natural nanomaterials, halloysite nanotubes (HNTs) have attracted a lot of research interests. HNTs combine the advantages of high surface area, large aspect ratio, empty lumen structure, abundant in surface hydroxyl groups, good biocompatibility, low cost, and good mechanical properties, which make them a good candidate as nanobiomaterials [1]. Geologically, HNTs are widely present in wetland tropical, subtropical regions, and weathering igneous rocks, especially in volcanic rocks. Therefore, HNTs are an economically viable material that can be easily mined and have the least risk to the environment [2]. Chemically, HNTs are a silicate mineral with a similar formula to kaolinite ($\text{Al}_2\text{Si}_2\text{O}_5(\text{OH})_4 \cdot n\text{H}_2\text{O}$). However, different from the platelet-like kaolin, HNTs exhibit a hollow tubular nanostructure with a large aspect ratio [3]. The morphology of HNTs is similar with carbon nanotubes in some extent, but HNTs are a type of natural and inorganic one-dimensional nanomaterials [4]. Depending on deposit conditions, the length of HNTs varies between several hundred nanometers and several micrometers. HNTs have tubular nanostructures with an outer diameter of 30–70 nm and an internal diameter of 10–30 nm [3]. The pore brought by the surface defects on HNTs is in 2–3 nm. The outer and inner surfaces of HNTs consist of siloxane groups and aluminol groups respectively, the surface

charge of HNTs is related to its environment, such as pH, ion strength and so on [5]. However, the positive charges of the inner surface have a very limited contribution to the charge of HNTs, and the determined zeta potential of HNTs is negative with ~ 20 mV.

HNTs have been extensively studied as drug delivery carrier, sensor, catalyst carrier, and polymer nanoreinforcement [6–9]. As drug delivery carrier, HNTs have low cytotoxicity and high adsorption ability towards drugs. HNTs can load and release a variety of biologically active molecules via adsorption and desorption process [10,11]. In recent years, there has significant progress in the employment of HNTs for drug delivery. For example, HNTs were grafted with chitosan for delivery of curcumin, which can achieve enhanced anti-cancer efficacy towards different cancer cells [4]. In another study, chemically modified cyclodextrin was grafted onto HNTs, which further was used as curcumin carrier [12]. For drug delivery application, HNTs must have good biocompatibility and cell affinity, so that surface modification is required, such as polymer grafting, silane conjugation and so on.

Because of the chemical stability and high conductivity, carbon materials are widely used in energy storage, capacitors, catalysis and biomedical fields [13–15]. Also, the prepared carbon nanoparticles are non-toxic, biocompatible and non-immune, which allows them to be widely used for intracellular drug delivery [16,17]. There are a variety of ways to synthesize carbon materials, such as chemical vapor

* Corresponding author.

E-mail address: liumx@jnu.edu.cn (M. Liu).

deposition, catalytic pyrolysis of organic compounds, and hydrothermal carbonization [18,19]. Recent research showed that carbon microspheres with different particle sizes could be prepared by hydrothermal carbonization of glucose [20]. The prepared carbon microspheres have excellent hydrophilicity and surface reactivity, so they can be used in the fields of biochemistry and biological diagnosis. The reaction conditions for hydrothermal carbonization are easy to operate, and hydrothermal carbonization can generate a variety attractive nanostructure from cheap and sustainable carbonaceous materials. It has been reported that the carbonaceous products can be obtained by hydrothermal carbonization of palm-empty fruit strings [21].

Compared with traditional carbonaceous materials, the combination of clay minerals and carbon can achieve economical and effective composites which show high adsorption ability and other functional properties [22]. Numerous clay@carbon composites have been synthesized by one-pot hydrothermal process of the polysaccharide solution in the presence of clay. In the course of the reaction, clays were used as the matrix, and glucose was usually used as a carbon source. In high temperature and water environment, glucose dehydrated to form furan and other molecules, followed by polymerization and carbonation. Generally, the hydrothermal carbonization results in the product of low degree crystallization (most of the carbon were amorphous), only a tiny amounts of carbon are graphitized [23]. Clays can inhibit the homogeneous nucleation effect during the carbonation process, and the carbonized product could be deposited on the surface of the clay surfaces to form functional materials [24]. The clay@carbon materials obtained from hydrothermal carbonization process at lower temperature possessed numerous active oxygen-containing groups on their surfaces and hence could be used as adsorbents such as water purification. For example, attapulgite@carbon nanocomposite possessed a higher adsorption capacity for the removal of Cr(VI) and Pb(II) ions in water with maximum adsorption capacities of 177.7 and 263.8 mg g⁻¹ [25,26]. The adsorption rate of HNTs@Carbon (HNTs@C) on Cr(VI) and other heavy metal ions was also greatly increased [27]. A carbon/manganese dioxide/HNTs hybrids were used as a supercapacitor, where HNTs were used as templates and can be eventually removed [28]. However, detailed carbonation conditions have not been systematically examined and the biocompatibility of the clay@carbon material was little evaluated.

Accordingly, the main goal of the present work is to provide a full understanding of the structural characteristics of HNTs@C and the relationships between the materials and the biocompatibility. HNTs@C nanocomposites were synthesized by one-step hydrothermal carbonization of glucose on the surface of HNTs. HNTs can effectively induce heterogeneous deposition of carbonaceous materials on their surfaces, which leads to a layer of amorphous carbon around HNTs. The effects of glucose loading and carbonization time on the structure of the composites were investigated. The hemolysis rate, protein adsorption, and cell compatibility of HNTs@C were also studied. After hydrothermal carbonization reaction, the surface of nanotubes has abundant hydroxyl and carboxyl groups [29]. Therefore, the adsorption properties and blood compatibility of HNTs increase, while the cytotoxicity reduces. The prepared HNTs@C is biocompatible clay nanomaterial that could be used as drug delivery carrier.

2. Experimental

2.1. Materials

HNTs were purchased from Guangzhou Runwo Materials Technology Co., Ltd., China. Before use, HNTs were purified according to the reference to remove impurities [30]. Glucose and anhydrous ethanol were purchased from Tianjin Damao Chemical Reagents Co., Ltd., China. Bovine serum albumin was purchased from Guangzhou Sijia biotech Co., Ltd., China. CCK8 reagents were purchased from BestBio biology Co., Ltd., China. Acridine orange (AO) and ethidium

bromide (EB) were purchased from Beijing Solarbio science & technology Co., Ltd., China. Ultrapure water was produced from a Milli-Q water system. All the other reagents were analytically graded and used without further purification.

2.2. Synthesis of HNTs@C nanocomposites

The carbon-wrapped HNTs@C nanocomposites were prepared by hydrothermal carbonation in an aqueous solution with HNTs and glucose [31]. In a typical procedure, 0.5 g of HNTs was dispersed in 40 mL of water by sonication. Then the different amount of glucose (1 g, 2.5 g, or 4 g) was dissolved in the dispersion. The mixed solution was separately transferred into a Teflon-lined stainless steel autoclave (50 mL). The container was sealed and maintained at 160 °C for 12–72 h. After cooling down to room temperature, the as-prepared black-brown precipitation was rinsed with ethanol and centrifuged for five times and freeze-dried. The product was denoted as HNTs@C with HNTs and glucose weight ratio. For example, the HNTs@C 1:2 meant the weight ratio HNTs and glucose was 1:2.

2.3. Characterization of HNTs@C

The microscopic morphology was observed by using transmission electron microscopy (TEM) (JEM-2100F, JEOL Ltd., Japan) under an accelerating voltage of 100 kV. The samples were ultrasonically dispersed in absolute ethanol and dropped onto a copper grid covered with a carbon film before observation. Scanning electron microscope (SEM) (Ultra-55, Carl Zeiss Jena Ltd., Germany) was operated at an accelerating voltage of 5 kV and high vacuum mode after coating the sample with a gold film. Surface functional groups were determined by Fourier transform infrared spectroscopy (FTIR) and tested using Thermo FTIR (Nicolet iS50, Thermo Fisher Scientific Ltd., USA). The spectrum was recorded from 4000 to 400 cm⁻¹ and was presented at transmittance mode. Powder X-ray diffraction (XRD) analysis was tested with X-ray diffractometer (MiniFlex-600, Rigaku Corporation, Japan). Energy Dispersive Spectrometer (EDS) analysis was analyzed at 200 kV by Field Emission Transmission Electron Microscope (JEOL 2100F, JEOL Ltd., Japan). X-ray photoelectron spectroscopy (XPS) analysis was analyzed by XPS instrument (ESCALAB250Xi, Thermo Fisher Scientific Ltd., USA). The atoms of Al, Si, C, N, and O were detected. The Brunauer–Emmett–Teller (BET) specific surface area and Barrett–Joyner–Halenda (BJH) pore analysis were implemented by automated surface area and pore size analyzer (BeiShiDe 3H-2000, Instrument-S & T.Co., Ltd., China). The adsorption and desorption curves were obtained simultaneously. Zeta potential of the HNTs, HNTs@C 1:2, HNTs@C 1:5, and HNTs@C 1:8 aqueous dispersion was measured using a NanoBrook Omni (Brookhaven Instruments Ltd., US) at the 25 °C. The dispersion was tested at pH of 7.8. For water contact angle measurement, the HNTs and HNTs@C (1:3) powders were compressed into tablets by tablet press and then in oven at 60 °C for 3 h. The 10 μL of purified water droplets were deposited on the surface of the dried tablet sample.

2.4. Hemocompatibility of HNTs@C

1 mL fresh rabbit blood was added into 15 mL PBS solution, then the mixture was centrifuged at 1000 rpm for 5 min and the supernatant was discarded. The operation was repeated for 3 times and red blood cells (RBCs) were collected. Then, 320 μL RBCs were added into 1680 μL PBS solution and formed a RBCs suspension [32]. Firstly, 500 mL ultrapure water and PBS solution were added into RBCs suspension as the positive control group and the negative control group. 25 μL of RBCs suspension was further added into 5 mL HNTs, HNTs@C 1:2, HNTs@C 1:5 and HNTs@C 1:8 PBS solution (0.5 mg mL⁻¹). All the samples were vibrated slightly and incubated at 37 °C for 1 h. After incubating, RBCs suspension was centrifuged at 1000 rpm for 5 min. Besides, the

supernatant was centrifuged at 15000 rpm for 5 min to eliminate the effect of materials. Then, the absorbance of the supernatant liquid was measured with microplate reader at 570 nm. The positive control group was 100% hemolysis and the negative control group was 0% hemolysis.

The hemolysis rate was calculated as follows equation.

$$\text{Hemolysis rate (\%)} = \frac{\text{sample absorbance} - \text{negative control}}{\text{positive control} - \text{negative control}} \times 100\%$$

2.5. BSA adsorption experiment

First, prepare a BSA solution with a concentration of 0, 10, 20, 40, 80 $\mu\text{g mL}^{-1}$, and the absorbance at 273 nm was tested using ultraviolet-visible spectrophotometry, respectively [33]. After that, a standard curve for BSA was obtained. Then, 1 g of BSA was dissolved in 50 mL of ultrapure water. Batch experiments were performed in a 15 mL centrifuge tube, each of them contained 10 mL of the above aqueous solution of BSA. Then, 0.1 g of HNTs, HNTs@C 1: 2, HNTs@C 1: 5 and HNTs@C 1: 8 were added to the centrifuge tube and dispersed by ultrasonic at the pH of 7. The centrifuge tube was placed on the shaker to absorb at 37 °C. The mixture was centrifuged at 15,000 rpm after 15 h and the absorbance of supernatant was measured.

2.6. Cell counting kit-8 (CCK-8) assays

HeLa cells (1×10^4 , cells/well) were seeded in a 96-well plates and cultured at 37 °C for 24 h, and then incubated with HNTs, HNTs@C 1:2, HNTs@C 1:5, and HNTs@C 1:8 at different concentrations (0, 10, 20, 40, 80 $\mu\text{g mL}^{-1}$) for 24 h. Then, the cells were washed twice with PBS and 100 mL fresh medium was added. After that, 10 μL CCK-8 reagents were added to each well and incubated for 4 h. The supernatant was centrifuged at 15,000 rpm to eliminate the effect of the material on the absorbance results. The absorbance was recorded at 450 nm by a microplate reader. The cell survival rate was the absorbance ratio of the sample to the control group.

2.7. AO/EB staining assay

HeLa cells (1×10^4 , cells/well) were seeded in a 96-well plates for 24 h, then a series of HNTs, HNTs@C 1:2, HNTs@C 1:5, and HNTs@C 1:8 (0, 10, 20, 40, 80 $\mu\text{g mL}^{-1}$) were added to per well and cultured for 24 h. After that, cells were stained by 10 μL mixtures of AO (100 $\mu\text{g mL}^{-1}$) and EB (100 $\mu\text{g mL}^{-1}$), and observed under the fluorescence microscope (XDY-2, Guangzhou Liss Optical Instrument Ltd., China).

3. Results and discussions

3.1. Characterization of the HNTs@C

The morphology of HNTs and HNTs@C was characterized by TEM and SEM. Fig. 1 shows the digital photographs, TEM and SEM images of HNTs and HNTs@C. It is clear that natural HNTs are the white powder (Fig. 1A), and HNTs show the hollow tubular structure in Fig. 1B. After the hydrothermal reaction with glucose, HNTs become brownish black powder, and tubes are wrapped by a layer of amorphous carbon. The color of the powder also changes from black to brown with the glucose concentration. HNTs can effectively inhibit the carbonation process in the homogeneous nucleation effect during the hydrothermal reaction process. On the other hand, HNTs serve as a template for the formation of carbon layer from glucose [34]. HNTs greatly restrain the homogeneous nucleation of carbon spheres during the hydrothermal processes. In the absence of a template, only micrometer sized carbon spheres were obtained (Fig. 1SI) [29,35]. When HNTs were uniformly dispersed in glucose solution, some glucose molecules were adsorbed

on the tubes due to the abundant pore structure of HNTs. Then, glucose molecules were polymerized and carbonized on HNTs surfaces and the layer thickness increase with reaction time. The carbon structure formation mechanism is very similar to the Te@carbon-rich composite nanocables via hydrothermal process [24]. With the increase of the amount of glucose, the morphological characteristics of HNTs@C nanocomposites change. For TEM image of HNTs@C 1:2, only a thin layer of carbon is wrapped around the tubes. With the increase in the amount of glucose, carbon is evenly covered the total tube surfaces. The tubes are covered with a thick layer of amorphous carbon in the HNTs@C 1:8 sample. It can be seen from Fig. 1C that the thickness of the carbon layer is 17 nm. Fig. 1D shows SEM images of HNTs and HNTs@C. It is clear that with the increase in glucose content, the tubes become thicker and longer. The carbon wrapping changes the appearance of HNTs from sharp walls to indistinct edges. The SEM results are in agreement with the TEM results. The weight ratio of HNTs and glucose at 1: 8 was chosen to study the relationships between the microstructure and reaction time in the following section because of the maximum thickness of the carbon layer among the groups.

Fig. 2 shows the TEM and SEM images of the morphology of HNTs@C 1:8 obtained at different reaction times. These images show clearly the growth process of carbon outside of HNTs. As time goes on, tubes become thicker and longer. From 24 h to 48 h, the increase of the thickness of the carbon layer is particularly remarkable. The diameter of the tube increases slowly from 48 h to 72 h, suggesting that the reaction is close to saturated.

Fig. 3A and B show the FTIR spectra of HNTs and HNTs@C at different ratio and reaction time. HNTs show absorption peaks at 3696 cm^{-1} and 3623 cm^{-1} which are assigned to the O-H stretching of inner-surface hydroxyl groups and O-H stretching of inner hydroxyl groups, respectively. The peaks around 1030 cm^{-1} and 910 cm^{-1} are assigned to the in-plane Si-O stretching and O-H deformation vibration of the internal hydroxyl groups. After HNTs are hydrothermally treated with glucose, some new absorption peaks could be seen in the HNTs@C. For example, the absorption peak at 1696 cm^{-1} is assigned to the carbonyl characteristic peak [27]. The peak around 2919 cm^{-1} belongs to CH_2 asymmetric stretching. With the increase of reaction time and loading of glucose, the intensity of the characteristic peaks of CH_2 and carbonyl increases. These new absorption peaks demonstrate that carbon is immobilized outside the tubes. The crystalline structure of HNTs@C samples was identified by XRD and is shown in Fig. 3C and D. The diffraction peak at 12° assigned to (001) plane of HNTs can be found in all samples, which indicates that the basic structure of HNTs does not change during hydrothermal carbonization. Compared with raw HNTs [36], the peaks of (001), (100), (002), (110), (003), (210), (300), exist in HNTs@C but become weak. This can be understood by that the carbonization of organic materials has wrapped on the surfaces of HNTs. With the increase in glucose concentration and reaction time, HNTs are wrapped a thicker and thicker layer of amorphous carbon. The results of XRD are in agreement with the previous TEM, SEM, and IR results. For further studying the chemical composition of HNTs@C, XPS and EDS analyses were carried out.

Fig. 4A shows the survey of XPS for HNTs and HNTs@C. The C 1s peak of carbon element of raw HNTs is attributed to the impurities of the HNTs. After treatment by glucose, the peak of C 1s becomes stronger and the peaks of oxygen, silicon, and aluminum become weaker. The content of the surface elements of the two materials changes significantly. The oxygen, aluminum, and silicon contents decrease from 22.0% to 10.1%, from 26.7% to 2.9%, and from 28.3% to 2.5%, respectively. The carbon content increases from 13.9% to 83.2%. Fig. 4C shows the high-resolution XPS spectra of oxygen, carbon, silicon, and aluminum elements. The binding energy for O 1s is 531.4 eV, which belongs to the oxide component in raw HNTs. The oxygen binding energy increases to 532.8 eV after hydrothermal method. The great differences in the binding energy of O 1s among HNTs and HNTs@C 1:8 suggest that the hydrogen bonding interactions occur. The

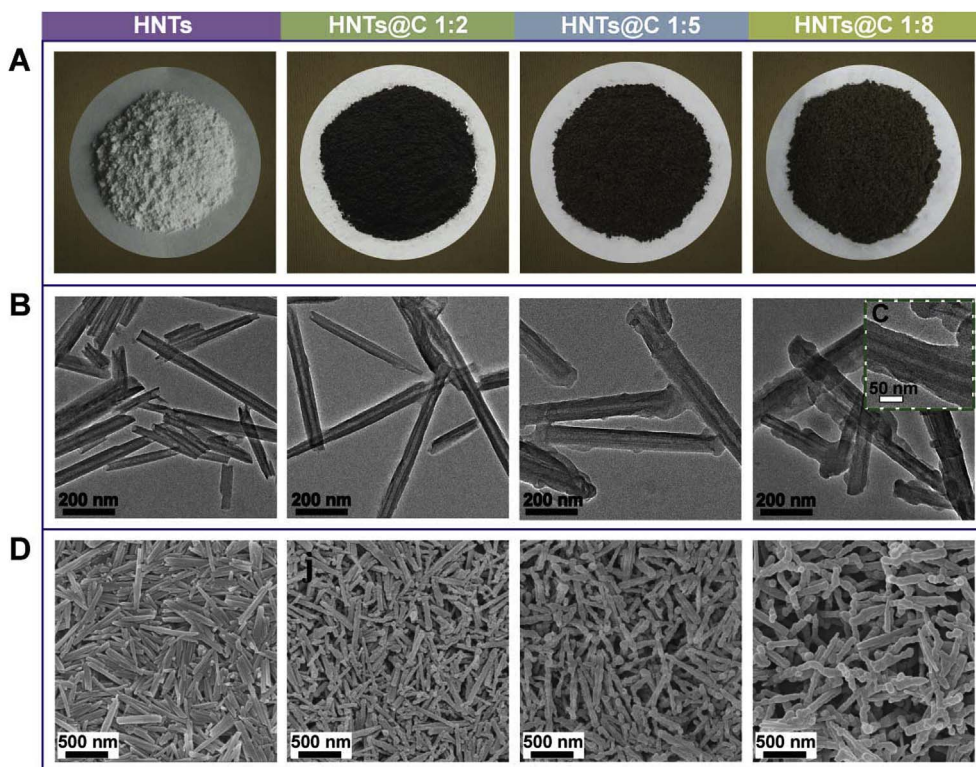


Fig. 1. Digital photos of (A) HNTs and different proportions of HNTs@C; TEM images of (B) HNTs and different proportions of HNTs@C; HRTEM image of (C) HNTs@C 1:8; SEM images of (D) HNTs and different proportions of HNTs@C.

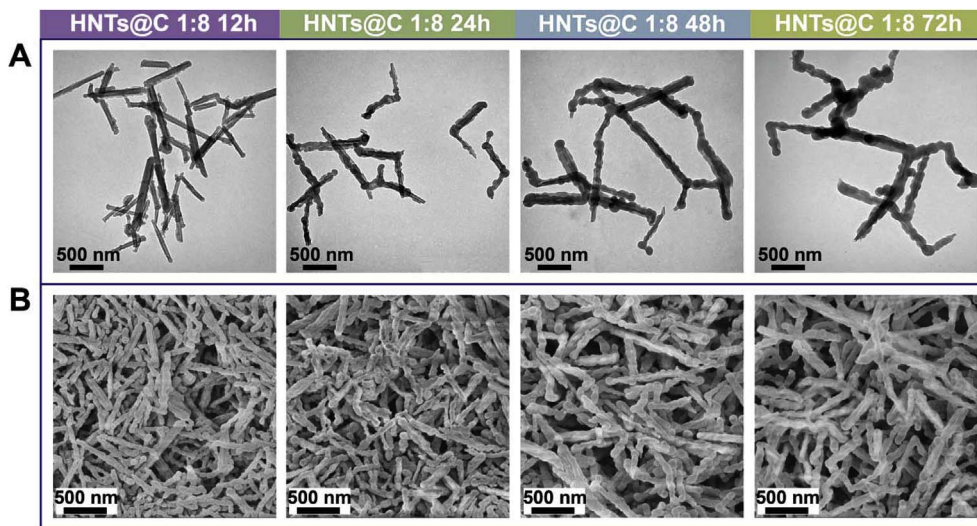


Fig. 2. TEM images of (A) HNTs@C 1:8 at different reaction times and SEM images of (B) HNTs@C 1:8 at different reaction times.

peak of C 1s at 284.8 eV is believed to signal the presence of adventitious elemental carbon [37]. The absence of movement of the C 1s indicates that no new chemical bonds are formed after modification. The binding energies for Si 2p and Al 2p of HNTs also move to high electron volts after modification. This is also due to the formation of hydrogen bonding interactions between the Si-O-Si and Al-O-Al group with carbon-containing organic groups by carbonization [38]. This further suggests that amorphous carbon is covered on the surfaces of HNTs, which leads to the decrease in silicon, aluminum and oxygen content and increase in carbon content [39]. Fig. 4B shows the EDS spectra of the HNTs@C 1:8. The elements of carbon, aluminum, silicon, and oxygen are detected from the surfaces of the tube. Although the use of a carbon film supported copper mesh in the EDS analysis can cause

some disturbances, the outline of the carbon around the HNTs is clearly visible (relatively dense pink points). We also attempted to perform the Raman analysis of the prepared HNTs@C samples. However, the carbon on the HNTs surfaces was burned immediately even at low power and short time laser irradiation during the Raman test. Therefore, no reliable data of Raman spectrum can be obtained. XPS and EDS results prove that the surfaces of HNTs are wrapped with a layer of abundant amorphous carbon.

Fig. 5 shows the size distribution of raw HNTs and HNTs@C in water. It should be noted that all HNTs and modified HNTs can be uniformly dispersed in water. The average size distribution of raw HNTs, HNTs@C 1:2, HNTs@C 1:5, HNTs@C 1:8 is 352.4 nm, 373.4 nm, 642.6 nm, and 693.7 nm, respectively. The increase in size is also

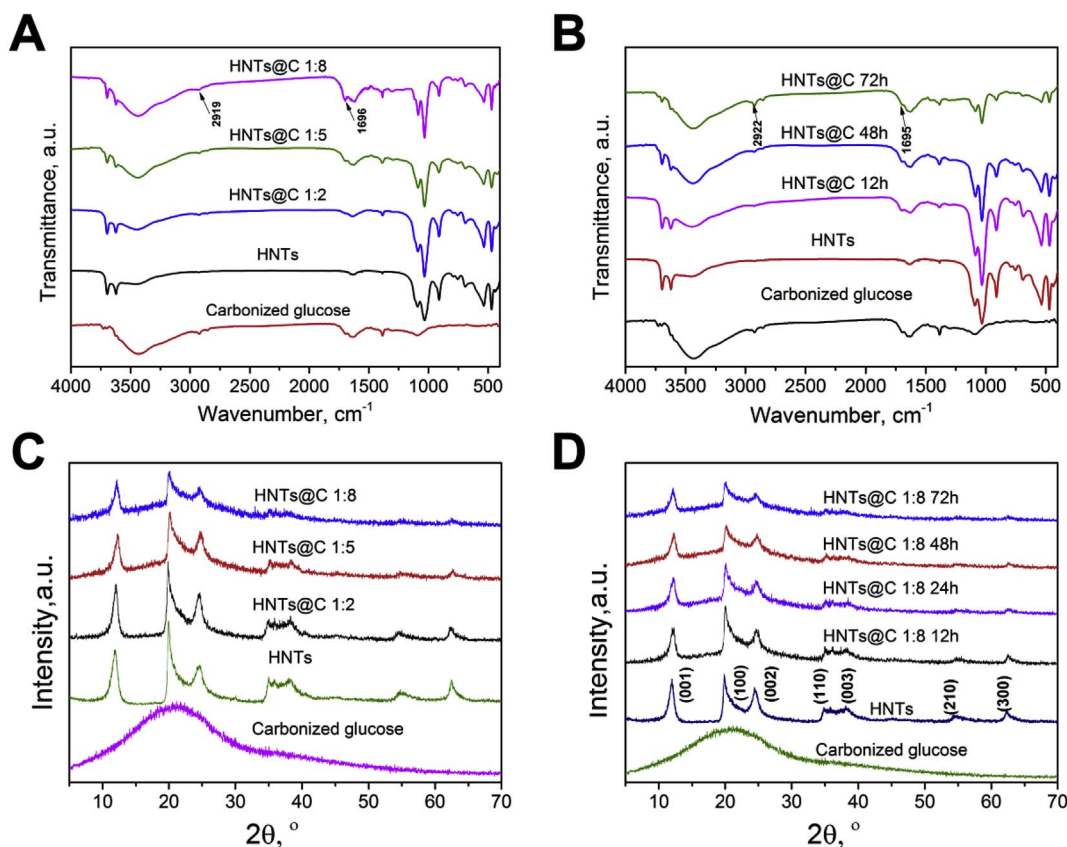


Fig. 3. FTIR spectra of HNTs and HNTs@C at different (A) glucose concentration and different (B) reaction time of HNTs@C 1:8; XRD pattern of HNTs and HNTs@C at different (C) glucose concentration and different (D) reaction time of HNTs@C 1:8.

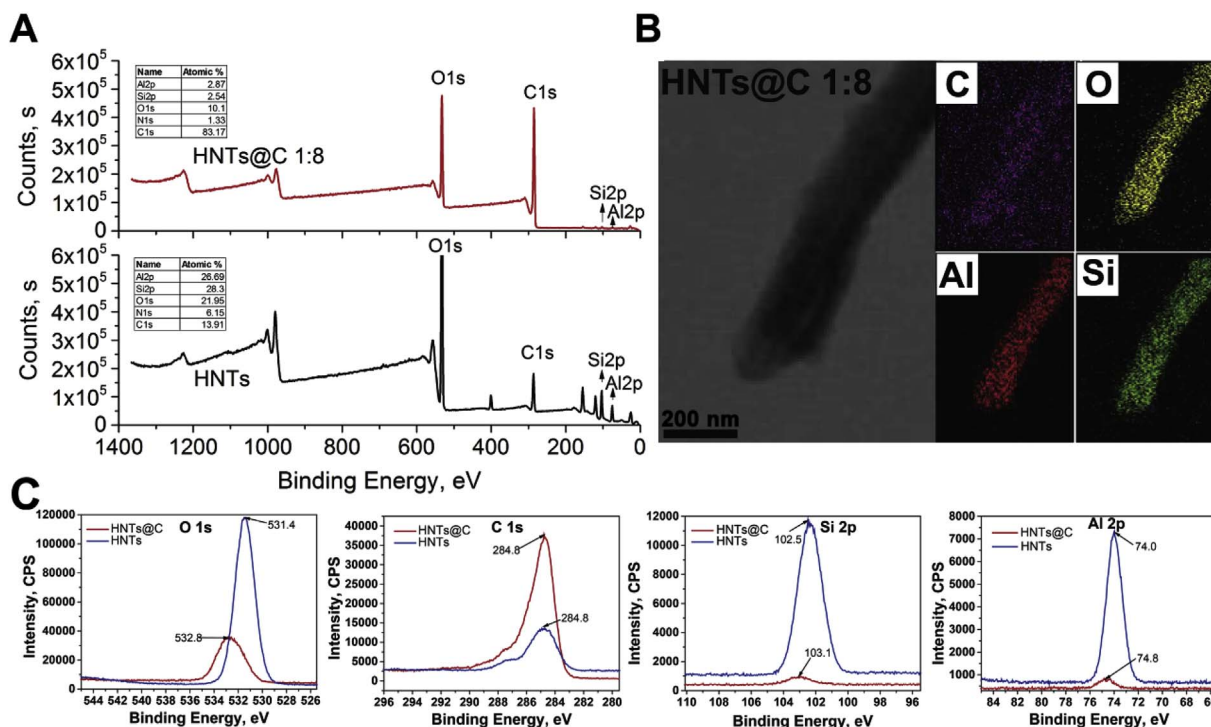


Fig. 4. The survey of (A) XPS spectra of HNTs and HNTs@C 1:8 and (C) high-resolution scanning of HNTs and HNTs@C 1:8; (B) EDS analysis of the HNTs@C 1:8.

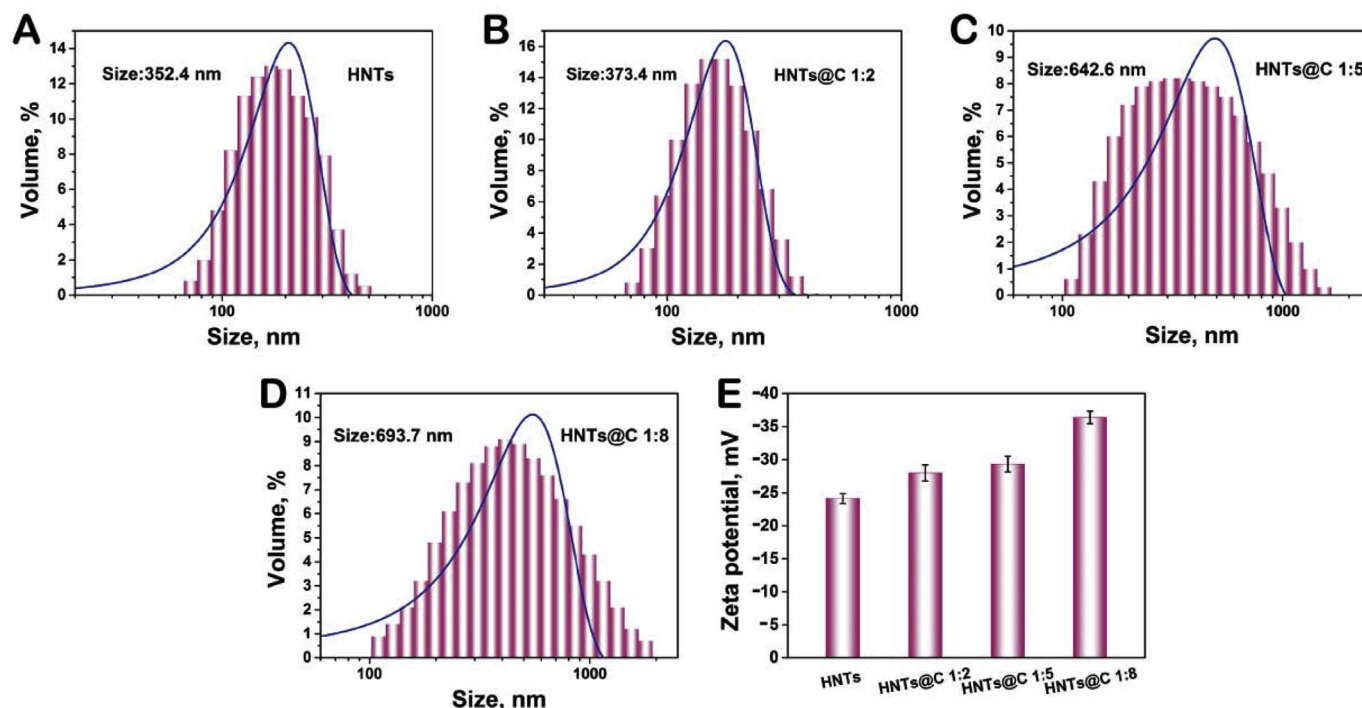


Fig. 5. DLS results of (A) HNTs, (B) HNTs@C 1:2, (C) HNTs@C 1:5 and (D) HNTs@C 1:8; (E) Zeta potentials of HNTs and HNTs@C.

attitude to the wrapping of carbon around HNTs. However, all HNTs@C is still in nanoscale. The size of HNTs measured by laser particle size analyzer differs from that measured by SEM or TEM technology. This is due to the fact that both technologies follow different principles. The laser particle size analyzer based on the principle of light scattering is more suitable for testing spherical particles. The charge properties of HNTs are further determined by zeta-potential measurement (Fig. 5E). The carbon microspheres prepared by hydrothermal carbonization are negatively charged since there are oxygen-containing groups on their surfaces [40]. When the concentration of glucose is low, HNTs are partly wrapped by carbon which leads to slightly increased negative charge of HNTs. As the carbon is completely wrapped on HNTs, the outer surface shows an increase in the negative charge. The increase in the zeta-potential of HNTs@C suggests that it also has good dispersibility in water. The water contact angles of HNTs increase from $11^\circ \pm 0.5$ to $36^\circ \pm 1^\circ$ after hydrothermal carbonization, revealing the slightly hydrophobic tendency of HNTs@C. It also has been reported that the contact angles of the carbon material prepared via hydrothermal carbonization increases and shows a hydrophobic tendency especially with long carbonization time due to the decrease in oxygen-containing functional groups and increase in carbon aromaticity structure [41].

Fig. 6A shows the nitrogen adsorption-desorption curves of HNTs and HNTs@C. Under the same relative pressure, the desorption value and adsorption value of HNTs@C are less than those of HNTs. The thicker the wrapped carbon is, the weaker is the adsorption capacity of nitrogen of HNTs@C. This is due to the shielding effect of amorphous carbon on HNTs surfaces. Other modifications of HNTs also lead to decreasing in the nitrogen adsorption ability of HNTs [42]. As expected, the BET specific surface of HNTs after modification decreases. The BET specific surface area of raw HNTs, HNTs@C 1:2, HNTs@C 1:5, HNTs@C 1:8 is determined as $49.43 \text{ m}^2 \text{ g}^{-1}$, $41.38 \text{ m}^2 \text{ g}^{-1}$, $36.98 \text{ m}^2 \text{ g}^{-1}$, $33.85 \text{ m}^2 \text{ g}^{-1}$, respectively. Fig. 6B shows BJH pore analysis of HNTs and HNTs@C. The pores of HNTs range from 2 to 120 nm, which indicates that mesopores and macropores are present simultaneously. The peaks around 3, 20, and 50 nm are attributed to surface defects of HNTs, the lumens of the nanotubes and the holes in the nanotubes,

respectively [43]. When the glucose concentration is low, HNTs are wrapped by amorphous carbon and the pore of 3 and 20 nm disappear leaving only 50 nm holes. As the glucose concentration increases, the pore around 50 nm is further covered. From nitrogen adsorption experiment, it is further concluded that HNTs are wrapped with a thick layer of amorphous carbon.

3.2. Biocompatibility and characterization of HNTs@C composites

For biomedical application such as a drug delivery platform, materials must have high hemocompatibility and good cytocompatibility [44]. Previous studies have demonstrated that raw HNTs have good cytocompatibility but poor blood compatibility. If the hemolysis rate is less than 5%, the medical material is considered to be non-hemolytic according to the national standard of hemolytic test. Therefore, hemocompatibility of HNTs and HNTs@C was evaluated by hemolysis analysis. Fig. 7A shows hemocompatibility of HNTs, HNTs@C 1:2, HNTs@C 1:5, and HNTs@C 1:8 at the concentration of $500 \mu\text{g mL}^{-1}$. Raw HNTs lead to an 80% hemolysis rate, which is related to the sharp and needle-like structure of the tubes which can harm the membrane of red blood cells. When the amorphous carbon is wrapped around the tubes, the hemolysis rate is rapidly reduced. With the increase in the thickness of the wrapped carbon layer, the hemolytic rate of HNTs@C decreases gradually. The HNTs@C 1:8 shows hemolytic rate of only 1.4%. This is attributed to the much rough surface characters of HNTs@C and the good hemocompatibility of carbon. Fig. 7B shows the protein adsorption behavior of HNTs before and after modification. With the increase of the glucose concentration, the adsorption capacity of BSA shows an increasing trend. The adsorption of BSA from HNTs@C 1:5 is greater than that of raw HNTs. The adsorption capacity of BSA HNTs@C 1:8 is 70% higher than that of raw HNTs.

HeLa cells were used as a model to assess the cytotoxicity of HNTs. HNTs can be taken up by the HeLa cells and allowed to safely be delivered into cells at high concentrations [45]. The cytotoxicity of HNTs@C is firstly evaluated by live/dead staining techniques. AO can enter the living cells to stain the nucleus with green luminescence, and EB can cause death and late apoptotic cells to emit light in orange.

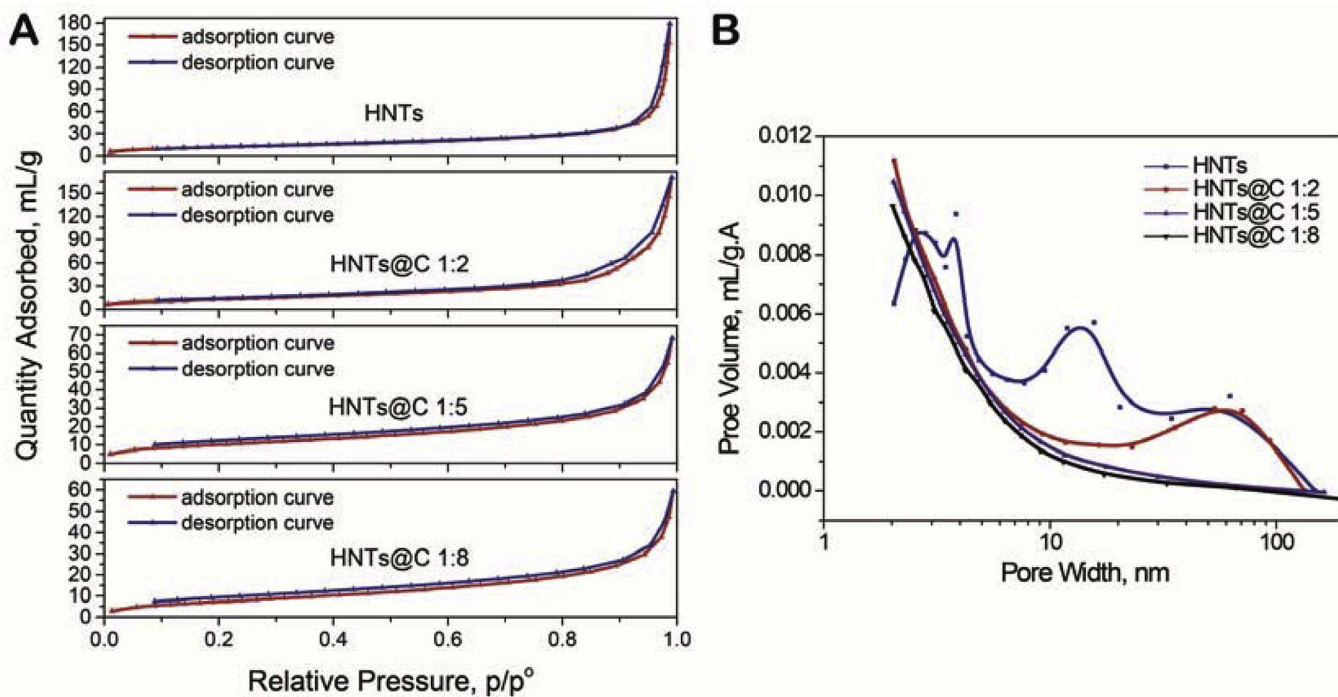


Fig. 6. (A) N₂ adsorption-desorption curves of HNTs and HNTs@C; (B) BJH pore analysis of HNTs and HNTs@C.

Fig. 8A shows fluorescence microscope images of HeLa cells treated with HNTs@C and HNTs in different concentration. It can be seen that some HeLa cells appear orange when the raw HNTs concentration is 20 mg mL⁻¹, indicating that some cells die. The orange of the cells gradually becomes darker with the increasing of HNTs concentration. This indicates an increase in cytotoxicity of the materials. With the same concentration, the orange cells in HNTs@C group are less than those of HNTs group. This suggests that the cytotoxicity of HNTs after modification decreases. The fluorescence microscope images of HeLa cells treated with HNTs@C and HNTs at 10 mg mL⁻¹ and 40 mg mL⁻¹ are shown in Fig. 2SI. Fig. 8B shows the CCK-8 assay result of the HeLa cells. The cytotoxicity of HNTs@C is less than that of pure HNTs. Among the groups, HNTs@C 1:5 shows the lowest toxicity. HNTs have stronger toxicity than HNTs@C at the same concentration. HNTs@C 1:8 shows comparable cytotoxicity with HNTs but increased cytotoxicity compared with HNTs@C 1:5. This is explained by the fact that the nanotubes in HNTs@C 1:8 become thicker and longer, and the tubes are easily deposited in the culture medium to cause apoptosis of cells.

Increased cytotoxicity is also found with the increase of HNTs and HNTs@C concentration. However, all the cells maintain a high-level viability larger than 80.8% when the concentration is less than 40 mg mL⁻¹. Fig. 8C shows the result of cell viability test of HNTs and HNTs@C towards HeLa cells with time. As the culturing time increase, the absorbance of all samples increases indicating that the cells grow well and the good cytocompatibility of the HNTs@C. The OD values of HNTs treated group are slightly lower than that of HNTs@C at the same concentration. The OD values of both HNTs and HNTs@C treated group are less than control group. This possibly may be attributed to the deposition of nanomaterials limits the growth of the cells. All these results indicate that HNTs@C with good cytocompatibility shows the promising application in biomedical areas, especially as drug delivery carrier.

4. Conclusions

A novel HNTs@C nanocomposite was synthesized by one-step

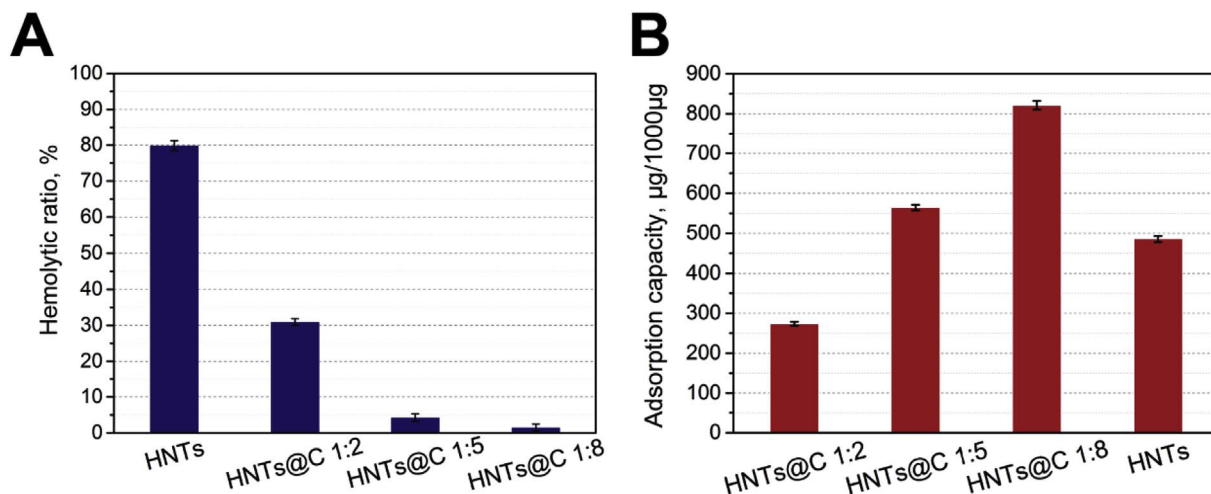


Fig. 7. Hemocompatibility of (A) HNTs and HNTs@C; the BSA adsorption capacity of (B) HNTs and HNTs@C.

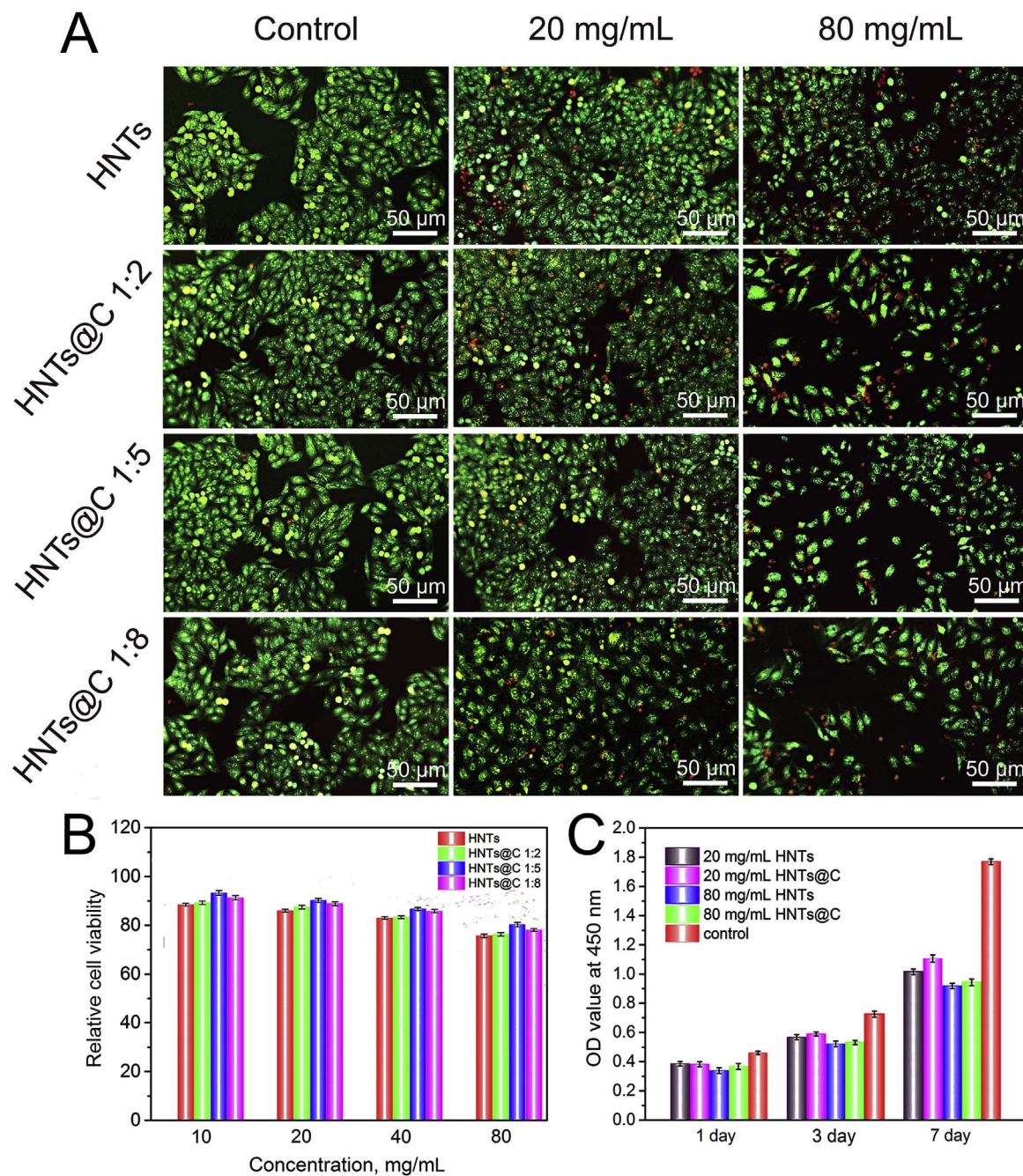


Fig. 8. The photos of AO/EB staining of (A) HeLa cells treated with HNTs and HNTs@C at the concentration of 0, 20, 80 (mg mL^{-1}) for 24 h; (B) the relative viability of HeLa cells after being treated with HNTs and HNTs@C at different concentration after 24 h; (C) The OD value of HeLa cells being treated with HNTs and HNTs@C after 1, 3 and 7 days. Data are shown as means \pm s.d. ($n = 4$).

hydrothermal carbonization of glucose on the surface of HNTs. The TEM and SEM images revealed that the carbon layer was successfully deposited on the surface of HNTs. BJH shows that the pores of HNTs were covered in the encapsulation of amorphous carbon. The thickest carbon layer was achieved when the HNTs and glucose ratio was 1: 8. The microstructure of HNTs@C changes slightly when the reaction time after 48 h. HNTs@C showed high hemocompatibility and cytocompatibility. BSA protein adsorption indicated that HNTs@C 1:8 could adsorb 70% higher BSA than that of raw HNTs. HNTs@C showed a hemolytic rate of less than 5%. In vitro cytotoxicity with HeLa cells showed a very low cytotoxicity of HNTs@C. All of these indicate that HNTs@C has potential applications in biomedical areas such as drug delivery carrier.

Acknowledgements

This work was financially supported by National High Technology Research and Development Program of China (2015AA020915), the National Natural Science Foundation of China (51473069 and 51502113), and the Guangdong Natural Science Funds for Distinguished Young Scholar (S2013050014606), Science and Technology Planning Project of Guangdong Province (2014A020217006), Guangdong Special support program (2014TQ01C127), and the Pearl River S&T Nova Program of Guangzhou (201610010026).

Appendix A. Supplementary data

Supplementary data related to this article can be found at <http://dx.doi.org/10.1016/j.micromeso.2018.02.027>.

References

- [1] M. Liu, Y. Zhang, C. Wu, S. Xiong, C. Zhou, *Int. J. Biol. Macromol.* 51 (2012) 566–575.
- [2] W. Chesworth, *Eur. J. Soil Sci.* 28 (1977) 490–497.
- [3] E. Joussein, S. Petit, J. Churchman, B. Theng, D. Righi, B. Delvaux, *Clay Miner.* 40 (2005) 383–426.
- [4] M. Liu, Y. Chang, J. Yang, Y. You, R. He, T. Chen, C. Zhou, *J. Mater. Chem. B* 4 (2016) 2253–2263.
- [5] E. Abdullayev, Y. Lvov, *J. Mater. Chem.* 20 (2010) 6681–6687.
- [6] Y. Lvov, W. Wang, L. Zhang, R. Fakhrullin, *Adv. Mater.* 28 (2016) 1227–1250.
- [7] X. Sun, Y. Zhang, H. Shen, N. Jia, *Electrochim. Acta* 56 (2010) 700–705.
- [8] Z. Yang, X. Zheng, J. Zheng, *RSC. Adv* 6 (2016) 58329–58335.
- [9] S. Barrientos-Ramírez, E.V. Ramos-Fernández, J. Silvestre-Albero, A. Sepúlveda-Escribano, M.M. Pastor-Blas, A. González-Montiel, *Microporous Mesoporous Mater.* 120 (2009) 132–140.
- [10] S.R. Levis, P.B. Deasy, *Int. J. Pharm.* 243 (2002) 125–134.
- [11] W. Li, D. Liu, H. Zhang, A. Correia, E. Makila, J. Salonen, J. Hirvonen, H.A. Santos, *Acta Biomater.* 48 (2017) 238–246.
- [12] M. Massaro, S. Riel, P.L. Meo, R. Noto, G. Cavallaro, S. Milioto, G. Lazzara, *J. Mater. Chem. B* 2 (2014) 7732–7738.
- [13] D.W. Wang, F. Li, M. Liu, G.Q. Lu, H.M. Cheng, *Angew. Chem. Int. Ed.* 47 (2008) 373–376.
- [14] P. Nikolaev, M.J. Bronikowski, R.K. Bradley, F. Rohmund, D.T. Colbert, K. Smith, R.E. Smalley, *Chem. Phys. Lett.* 313 (1999) 91–97.
- [15] H. Chen, M.B. Müller, K.J. Gilmore, G.G. Wallace, D. Li, *Adv. Mater.* 20 (2008) 3557–3561.
- [16] A. Yan, B.W. Lau, B.S. Weissman, I. Külaots, N.Y. Yang, A.B. Kane, R.H. Hurt, *Adv. Mater.* 18 (2006) 2373–2378.
- [17] T.-W. Kim, P.-W. Chung, I.I. Slowing, M. Tsunoda, E.S. Yeung, V.S.-Y. Lin, *Nano Lett.* 8 (2008) 3724–3727.
- [18] A. Eftekhari, P. Jafarkhani, F. Moztarzadeh, *Carbon* 44 (2006) 1343–1345.
- [19] L. Gherghel, C. Kübel, G. Lieser, H.-J. Räder, K. Müllen, *J. Am. Chem. Soc.* 124 (2002) 13130–13138.
- [20] J. Ryu, Y.-W. Suh, D.J. Suh, D.J. Ahn, *Carbon* 48 (2010) 1990–1998.
- [21] G.K. Parshetti, S.K. Hoekman, R. Balasubramanian, *Bioresour. Technol.* 135 (2013) 683–689.
- [22] J. Tang, B. Mu, L. Zong, M. Zheng, A. Wang, *Chem. Eng. J.* 322 (2017) 102–114.
- [23] S. Kang, X. Li, J. Fan, J. Chang, *Ind. Eng. Chem. Res.* 51 (2012) 9023–9031.
- [24] H.-S. Qian, S.-H. Yu, L.-B. Luo, J.-Y. Gong, L.-F. Fei, X.-M. Liu, *Chem. Mater.* 18 (2006) 2102–2108.
- [25] L.-F. Chen, H.-W. Liang, Y. Lu, C.-H. Cui, S.-H. Yu, *Langmuir* 27 (2011) 8998–9004.
- [26] Z. Feng, D. Liu, X. Ma, *Chemosphere* 144 (2016) 621–627.
- [27] X. Tian, W. Wang, N. Tian, C. Zhou, C. Yang, S. Komarneni, *J. Hazard Mater.* 309 (2016) 151–156.
- [28] W. Zhang, B. Mu, A. Wang, *Ionics* 21 (2015) 2329–2336.
- [29] M. Sevilla, A.B. Fuertes, *Carbon* 47 (2009) 2281–2289.
- [30] M. Liu, B. Guo, Q. Zou, M. Du, D. Jia, *Nanotechnology* 19 (2008) 205709.
- [31] W. Zhang, B. Mu, A. Wang, *J. Solid. State Electrochem.* 19 (2015) 1257–1263.
- [32] H.-Y. Liu, L. Du, Y.-T. Zhao, W.-Q. Tian, *J. Nanomater.* 2015 (2015) 1–9.
- [33] P.K. Smith, R.I. Krohn, G.T. Hermanson, A.K. Mallia, F.H. Gartner, M.D. Provenzano, E.K. Fujimoto, N.M. Goeke, B.J. Olson, D.C. Klenk, *Anal. Biochem.* 150 (1985) 76–85.
- [34] H.S. Kambo, A. Dutta, *Renew. Sustain. Energy Rev.* 45 (2015) 359–378.
- [35] X. Sun, Y. Li, *Angew. Chem. Int. Ed.* 43 (2004) 597–601.
- [36] W. Jinhua, Z. Xiang, Z. Bing, Z. Yafei, Z. Rui, L. Jindun, C. Rongfeng, *Desalination* 259 (2010) 22–28.
- [37] C. Li, J. Wang, S. Feng, Z. Yang, S. Ding, *J. Mater. Chem.* 1 (2013) 8045–8054.
- [38] X. Wu, C. Liu, H. Qi, X. Zhang, J. Dai, Q. Zhang, L. Zhang, Y. Wu, X. Peng, *Appl. Clay Sci.* 119 (2016) 284–293.
- [39] M. Liu, B. Guo, M. Du, X. Cai, D. Jia, *Nanotechnology* 18 (2007) 455703.
- [40] B. Hu, K. Wang, L. Wu, S.H. Yu, M. Antonietti, M.M. Titirici, *Adv. Mater.* 22 (2010) 813–828.
- [41] C. He, A. Giannis, J.-Y. Wang, *Appl. Energy* 111 (2013) 257–266.
- [42] J. Jin, Y. Zhang, J. Ouyang, H. Yang, *Phys. Chem. Miner.* 41 (2014) 323–331.
- [43] Y. Joo, J.H. Sim, Y. Jeon, S.U. Lee, D. Sohn, *Chem. Commun.* 49 (2013) 4519–4521.
- [44] J.M. Anderson, *Annu. Rev. Mater. Res.* 31 (2001) 81–110.
- [45] R. Yendluri, Y. Lvov, M.M. de Villiers, V. Vinokurov, E. Naumenko, E. Tarasova, R. Fakhrullin, *J. Pharm. Sci.* 106 (2017) 3131–3139.